

## Article

# Citric-Acid-Assisted Preparation of Biochar Loaded with Copper/Nickel Bimetallic Nanoparticles for Dye Degradation

Jessim Omiri<sup>1</sup>, Youssef Snoussi<sup>1</sup>, Arvind K. Bhakta<sup>1,2</sup>, Stéphanie Truong<sup>1</sup>, Souad Ammar<sup>1</sup> ,  
Ahmed M. Khalil<sup>1,3</sup> , Mohamed Jouini<sup>1</sup> and Mohamed M. Chehimi<sup>1,\*</sup> 

<sup>1</sup> Université de Paris, CNRS, ITODYS (UMR 7086), 75013 Paris, France; jessim.omiri@etu.u-paris.fr (J.O.); snoussi.youssef.24@gmail.com (Y.S.); arvindk.bhakta@gmail.com (A.K.B.); stephanie.lau@univ-paris-diderot.fr (S.T.); ammarmer@univ-paris-diderot.fr (S.A.); akhalil75@yahoo.com (A.M.K.); jouini@univ-paris-diderot.fr (M.J.)

<sup>2</sup> Department of Chemistry, St. Joseph's College, Karnataka, Bangalore 560 027, India

<sup>3</sup> Photochemistry Department, National Research Centre (NRC), Dokki, Giza 12622, Egypt

\* Correspondence: mohamed.chehimi@cnrs.fr

**Abstract:** Immobilization of nanocatalysts on biochar is receiving unprecedented interest among material and catalysis scientists due to its simplicity, versatility, and high efficiency. Herein, we propose a new direct approach to obtain bimetallic copper/nickel nanoparticles loaded on olive stone biochar. The bimetallic-coated biochar and the reference materials, namely bare biochar, copper rich-loaded biochar, and nickel-loaded biochar, were prepared by pyrolysis from olive pit powder particles impregnated first with citric acid (CA) and then with copper and nickel nitrates at 400 °C under nitrogen flow. We employed citric acid in the process in order to examine its effect on the structural and textural properties of biochar supporting the metallic nanoparticles. Surprisingly, citric acid induced the formation of agglomerated or even raspberry-shaped bimetallic copper/nickel nanoparticles. Large 450–500 nm agglomerates of ~80 nm bimetallic CuNi NPs were noted for B-CA@CuNi. Interestingly, for biochar material prepared with initial Cu/Ni = 10 molar ratio (B-CA@CuNi<sub>10/1</sub>), the bimetallic NPs formed unusual nanoraspberries (174 ± 8 nm in size), which were agglomerates of individual 10–20 nm CuNi<sub>10/1</sub> nanoparticles. The B-CA@CuNi and reference materials were characterized by Raman spectroscopy, scanning electron microscopy (SEM)/energy-dispersive X-ray spectroscopy (EDX), X-ray diffraction (XRD), and magnetometry. The B-CA@CuNi and B-CA@Ni materials could be efficiently attracted with a magnet but not B-CA@CuNi<sub>10/1</sub> due to the low nickel loading. B-CA@CuNi was tested as a catalyst for the degradation of methyl orange (MO). Discoloration was noted within 10 min, much faster than a similar material prepared in the absence of CA. B-CA@CuNi could be recycled at least 3 times while still exhibiting the same fast catalytic discoloration performance. This paper stresses the important role of citric acid in shaping bimetallic nanoparticles loaded in situ on biochar during the slow pyrolysis process and in enabling faster catalytic discoloration of organic dye solution.

**Keywords:** *Olea europaea*; olive stone; agro-waste; citric acid; slow pyrolysis; biochar; bimetallic nano-alloys; catalyzed dye degradation; trash-to-treasure



**Citation:** Omiri, J.; Snoussi, Y.; Bhakta, A.K.; Truong, S.; Ammar, S.; Khalil, A.M.; Jouini, M.; Chehimi, M.M. Citric-Acid-Assisted Preparation of Biochar Loaded with Copper/Nickel Bimetallic Nanoparticles for Dye Degradation. *Colloids Interfaces* **2022**, *6*, 18. <https://doi.org/10.3390/colloids6020018>

Academic Editor: Jaroslav Katona

Received: 16 February 2022

Accepted: 18 March 2022

Published: 22 March 2022

**Publisher's Note:** MDPI stays neutral with regard to jurisdictional claims in published maps and institutional affiliations.



**Copyright:** © 2022 by the authors. Licensee MDPI, Basel, Switzerland. This article is an open access article distributed under the terms and conditions of the Creative Commons Attribution (CC BY) license (<https://creativecommons.org/licenses/by/4.0/>).

## 1. Introduction

One way to valorize agro-waste is via pyrolysis into biochar [1] under inert atmosphere or in the presence of very low amount of air [2–4]. Biochar is nowadays a very hot research topic because it arises from the trash-to-treasure concept [5,6] and thus falls within the general domain of sustainable development [7]. Much has been said on the preparation of biochar [8] and control of its composition [9], graphitization degree [10], and porosity [11], among other features [2,12,13]. Moreover, biochar could even be employed as a source for obtaining novel graphene or carbon dots [14,15] as well as carbon nanotubes [16]. However, in recent years, it has been realized that biochar could be engineered using additives during

its preparation or after the carbonization process. For example, numerous papers have reported on grafting of molecular [17] or macromolecular species [18] to biochar supports or designed biochar decorated with metal oxide [19] and metallic nanoparticles [20–22]. Some authors have proposed decorating biochar with bacteria for soil amendment [23]. Its applications [24] encompass hydrogen evolution reaction and water splitting [25], removal of chromium VI [20], catalyzed degradation of dyes [26], soil remediation [27], electrochemical energy storage [28], design of support for N-fertilizers [29], and reducing phosphorous loss [30], to name a few.

Recently, we proposed a simple way to obtain biochar loaded with copper/nickel bimetallic nanoparticles (B@CuNi) [21]. The rationale for fabricating bimetallic CuNi NPs on biochar lies with the interest in this low-cost, magnetic, bimetallic nanomaterial in the catalysis of nitrate reduction [31,32], reduction of Cr(VI) to Cr(III) [33], oxygen evolution and reduction reactions [34], or degradation of nitrophenol and organic dyes [35]. When directly coated on biochar during pyrolysis, CuNi bimetallic NPs were found to be 10–20 nm in size and uniformly dispersed over the biochar surface [21]. The composite material was found to be magnetic and could catalyze the degradation of methyl orange (MO) within 30 min [21].

In order to increase the porosity of the underlying biochar, one could pyrolyze the initial agro-waste by modifying with carbonates or oxalates but also carboxylic acids, such as citric acid. For example, incorporation of citric acid monohydrate followed by fixation of  $K^+$  ions via ion exchange with KOH and then carbonization at elevated temperature resulted in biochar with micropores [36,37]. A study was carried out to understand the effect of various potassium-containing compounds for porous carbons. Mixing of rice husk biomass with these compounds via ball milling followed by heating caused catalytic pyrolysis with the following decreasing order:  $KOH > K_2CO_3 > K_2C_2O_4$  [38]. Bridging the gap with our ongoing research work, one could expect the tricarboxylic group from citric acid to play a crucial role in bi- and trivalent metal ion complex formation [39].

In our protocol [21], wet impregnation of agro-waste powder prior to pyrolysis ensured remarkable distribution of the dispersed bimetallic nanoparticles. Therefore, we reasoned that it is beneficial to impregnate the biomass with citric acid prior to addition of copper and/or nickel nitrates and thus investigate the effect of citric acid on the properties of the biochar and the supported nanoparticles. Surprisingly, scanning electron microscopy (SEM) imaging revealed the deposition of agglomerated nanoparticles and some were even found to be raspberry-shaped, which is quite unusual and thus worthy of reporting. Indeed, to the very best of our knowledge, no previous study has considered combining carboxylic acid treatment of biomass for the deposition of bimetallic nanoparticles, hence motivating us to carry out this work.

Herein, we report on the preparation of olive pit biochar loaded with copper/nickel bimetallic nanoparticles by slow pyrolysis at 400 °C. The initial agro-waste powder was first impregnated with citric acid (CA) and then loaded with copper and nickel nitrates prior to pyrolysis. The final citric-acid-impregnated OP biochar (B) loaded with bimetallic copper/nickel (B-CA@CuNi) and the reference materials B-CA, B-CA@CuNi<sub>10/1</sub>, and B-CA@Ni were characterized by scanning electron microscopy (SEM)/energy-dispersive X-ray spectroscopy (EDX), X-ray diffraction (XRD), and Raman and magnetization measurements employing superconducting quantum interference device (SQUID). The final B-CA@CuNi was tested as a potential catalyst for the degradation of methyl orange (MO) dye, which was taken as a model organic pollutant.

## 2. Experimental

### 2.1. Chemicals

Olive pit (OP) powder (grain diameter from 40 to 600  $\mu m$  [40]) was obtained after extraction of Tunisian olive oil (see details in [21]). Citric acid (CA), metal nitrate salts,  $Cu(NO_3)_2 \cdot 3H_2O$  and  $Ni(NO_3)_2 \cdot 6H_2O$ , sodium hydroborate ( $NaBH_4$ ), and methyl orange (MO) were purchased from Aldrich and used as received. We used distilled water to

dissolve citric acid and the metal nitrates prior to pyrolysis and to prepare aqueous solutions for the dye degradation tests.

## 2.2. Preparation of Bare and Nanocatalyst-Modified Biochar Materials

OP particles were impregnated with an aqueous CA solution in the nominal ratio of 1 mmol CA/1 g OP using a minimal amount of water (see Table 1). The powder was dried at 70 °C and mixed thoroughly with a spatula. The same CA-loaded OP powder was impregnated again with a mixture of  $\text{Cu}(\text{NO}_3)_2 \cdot 3\text{H}_2\text{O}$  and/or  $\text{Ni}(\text{NO}_3)_2 \cdot 6\text{H}_2\text{O}$  (1 mmol each per 1 g of OP). Additionally, we prepared a biochar loaded with metallic nanoparticles from a 10/1 initial molar ratio of  $\text{Cu}(\text{NO}_3)_2 \cdot 3\text{H}_2\text{O}/\text{Ni}(\text{NO}_3)_2 \cdot 6\text{H}_2\text{O}$ . The mixture containing CA-impregnated OP and copper and nickel nitrates was left to dry overnight, then thoroughly mixed, dried again, and ground in agate mortar. It was weighed several times and mixed until the weight was stable.

**Table 1.** Experimental conditions for the preparation of impregnated biomass and the corresponding biochar.

Materials	OP Mass $\pm 0.0001$ (g)	OP Mass After Impregnation $\pm 0.0001$ (g)	CA Mass $\pm 0.0001$ (g)	$\text{Cu}(\text{NO}_3)_2 \cdot 3\text{H}_2\text{O}$ Mass (g)/mmol	$\text{Ni}(\text{NO}_3)_2 \cdot 6\text{H}_2\text{O}$ Mass (g)/mmol	Pyrolyzed OP Impregnated with Metal Ions (g)	Biochar Mass (g) and Yield (%)	Final Metal/ Biochar Ratio (mmol/g)
OP + CA	3.0000	3.5762	0.5762	-	-	0.7750	0.220 (28.4%)	-
OP + CA + CuNi	3.0010	5.1750	0.5760	0.7250/3.000	0.8730/3.002	0.8010	0.246 (30.7%)	3.776 mmol/g
OP + CA + CuNi (10/1)	3.0060	4.4045	0.5775	0.7245/2.999	0.0965/0.332	0.7960	0.254 (31.9%)	2.37 mmol/g
OP + CA + Ni +	3.0093	4.4586	0.5760	-	0.8733/3.003	0.8010	0.269 (33.6%)	2.30 mmol/g

Water volume for impregnation of citric acid = 20 mL and for impregnation of nitrates = 20 mL. Pyrolysis conditions = 30 °C/min;  $T_{\text{max}}$  = 400 °C; time at  $T_{\text{max}}$  = 2 h.

Visually, the OP powder changed color upon impregnation with CA and further with the metal nitrates (this is detailed below in Section 3). About 0.8 to 1 g of impregnated olive pit particles were pyrolyzed under  $\text{N}_2$  stream for 2 h at 400 °C in a tubular furnace. The apparatus was stopped for cooling but kept under  $\text{N}_2$  flow in order to avoid oxidation and ash formation.

The experimental conditions for preparing the impregnated biomass and pyrolysis are reported in Table 1.

## 2.3. Characterization

X-ray diffraction (XRD) patterns of the biochar samples were acquired with an X'Pert-Pro Analytical diffractometer fitted with a Cobalt X-ray source ( $\lambda = 1.7889 \text{ \AA}$ ) and operating in the Bragg–Brentano reflexion geometry (tube current = 40 mA and operating voltage = 40 kV).

Raman spectra of the biochar specimens were recorded using a Horiba HR 800 instrument, with the wavelength of the He–Ne laser beam set to 633 nm.

SEM observations and EDX spectral acquisition were performed on a Gemini SEM 360.

The magnetic properties of the produced catalysts were measured by a Quantum Design physical property measurement system (PPMS). Typically, the dc-magnetization  $M$  was measured by cycling the magnetic field  $\mu_0 H$  between +7 and −7 T at room temperature (300 K). The diamagnetic contribution of the biochar was then subtracted from the recorded  $M(\mu_0 H)$  data before being plotted for the Ni-based catalysts and expressed per gram of catalyst.

## 2.4. Catalytic Degradation of Methyl Orange

Here, 1 mg of catalyst was added to a beaker containing 4 mL of 20 ppm aqueous dye solution. The beaker was sonicated for 2 min, and 30 mg of  $\text{NaBH}_4$  was then poured in the beaker in order to trigger catalysis. A strong magnet was placed near the beaker to attract the biochar and sample sufficient MO solution for UV–vis analysis. Typically, the decrease in MO concentration was monitored using a Perkin Elmer-Lambda 1050 spectrophotometer

operating in the transmission mode (optical length of 1 cm). The optical absorption spectra of the reaction solution containing MO were recorded in the 200–800 nm range.

### 3. Results and Discussion

Figure 1 displays the main steps in the preparation of biochar materials from the biomass (Figure 1a) and the digital photographs of the materials (Figure 1b). Wet impregnation by citric acid and by the nitrates ensured uniform impregnation prior to pyrolysis, as can be noted from the digital picture. All metallic nanoparticle-coated biochar looked the same, so only B-CA@CuNi is shown for the sake of simplicity.

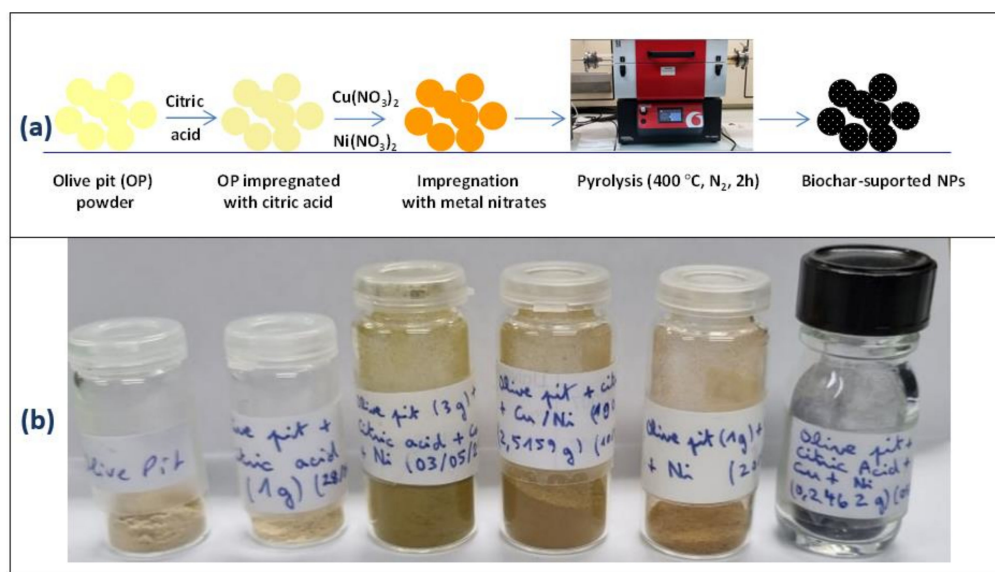


**Figure 1.** (a) General pathway for the design of biochar materials and (b) digital photographs of OP grains before and after impregnation with citric acid and copper/nickel nitrates (in three proportions) leading to black biochar composite powder.

#### 3.1. Physicochemical Properties of Biochar Nanocomposites

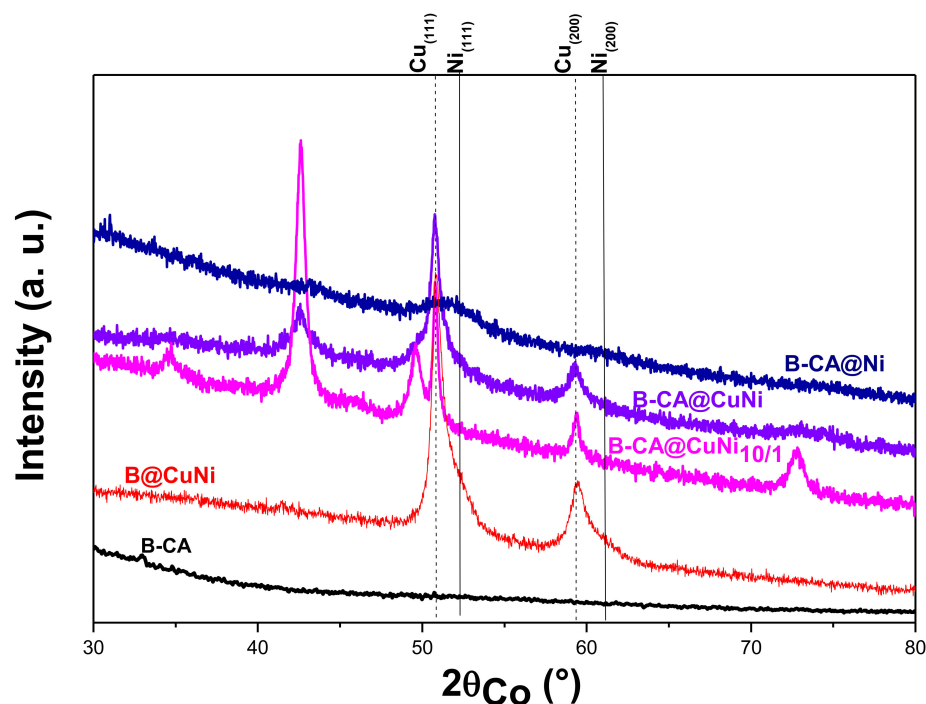
##### 3.1.1. Structural Analysis Studies by XRD and Raman Spectroscopy

Figure 2 displays the XRD patterns of B-CA-based catalysts, B-CA, and B@CuNi prepared without any CA. The diffraction peak positions were compared to those tabulated for Cu and Ni and their oxides. The (111) and (200) planes of the metallic phases are indicated by dashed (Cu) or solid (Ni) black vertical lines.

The amorphous nature of the underlying carbon substrate is evidenced by the featureless pattern of the metal-free B-CA sample. In contrast, the Cu- and/or Ni-loaded samples exhibited broadened peaks at  $2\theta$ . For some of them, the position matched those tabulated for bulk Cu (ICDD n°98-005-2256) and/or Ni (ICDD n°98-004-1508). This means that the produced metallic particles were very small in size and partially oxidized. Additionally, the presence of organic acid during material processing seemed to lead to the formation of metallic crystals that were smaller in size than those prepared from the same metal nitrates but without any CA [21]. In particular, the most nickel-rich particles were much smaller and thus much more sensitive to oxidation upon air exposure (see Table 2).

The peak broadening did not show evidence of a net shift of the peak position to confirm the formation of  $\text{Cu}_{1-x}\text{Ni}_x$  solid solution. However, NiO and  $\text{Cu}_2\text{O}$  phases being identified in the recorded patterns for all produced B-CA-based catalysts was in disagreement with the hypothesis. The use of CA clearly induced cation complexation over the whole OP surface, possibly for the nickel cations much more than the copper ones, which led to increased metal nucleation sites during pyrolysis and therefore generated very small metal crystals. The differences in affinities between each type of cation and citric acid contributed to the segregation of their related metallic phases. This feature was not at

all relevant when catalyst synthesis proceeded without CA. Indeed, the XRD pattern of B@CuNi was much more similar to the signature large-sized Cu- and Ni-rich  $\text{Cu}_{1-x}\text{Ni}_x$  solid solution crystals, with peak positions slightly comparable to those tabulated for pure Cu and pure Ni, respectively [21].



**Figure 2.** XRD patterns of B-CA@CuNi, B-CA@CuNi<sub>10/1</sub>, and B-CA@Ni compared to those of metal-free B-CA and CA-free B@CuNi<sub>1/1</sub> samples.

**Table 2.** Metal and metal oxide weight ratio and crystal size inferred from diffraction peak intensity and broadening <sup>a</sup>.

Catalyst	Crystal Phase	Phase Content (wt.%)	Crystal Size (Å)	Ref.
B-CA@Ni	Ni	30	30	This work
	NiO	70	60	
B-CA@CuNi	Cu	48	130	
	Cu <sub>2</sub> O	12	125	
	Ni	10	40	
B-CA@CuNi <sub>10/1</sub>	NiO	30	75	
	Cu	67	120	
	Cu <sub>2</sub> O	21	110	
B@CuNi	Ni	10	40	[21]
	NiO	2	60	
	Cu	70	190	
	Ni	30	40	

<sup>a</sup> Hypothesis: isotropic shapes are expected for all catalysts prepared in the presence of CA but not for B@CuNi<sub>1/1</sub> catalyst produced without any pre-impregnation of OP with CA.

To summarize, citric acid is most probably prone to provide ultrafine metallic NPs, which get oxidized upon air exposure. This oxidation is not so critical as the metallic phase can be easily recovered by adding sodium borohydride ( $\text{NaBH}_4$ ) during catalysis assays.

To complete the copper/nickel structural investigations, the Raman spectra of all the produced composites were recorded to characterize the biochar support (Figure 3).

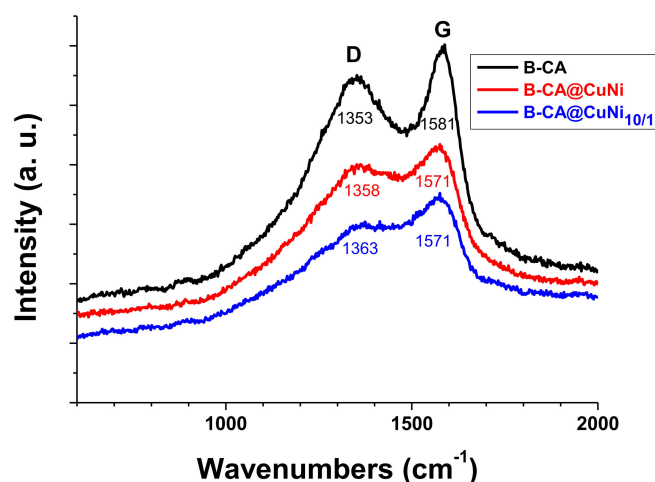


Figure 3. Raman spectra of B-CA, B-CA@CuNi, and B-CA@CuNi<sub>10/1</sub>.

Interestingly, all spectra exhibited doublet characteristic of carbon-based materials. Indeed, two peaks, coined D and G, were centered at  $1351 \pm 1$  and  $1576 \pm 5$   $\text{cm}^{-1}$ , respectively (Figure 3) [41]. The D band accounted for defects in the biochar chemical structure, for example, C–C bonds between aromatic rings [42] and C–O defects [41]. The G band was assigned to aromatic ring breathing and C=C bonds. The D/G intensity ratio (peak height ratio) was in the 0.79–0.89 range, which was higher than the 0.67 obtained for the same biochar prepared under slightly different conditions at 400 °C under N<sub>2</sub>/H<sub>2</sub> mixture [21] and also higher than the 0.58 obtained for Spanish olive stones carbonized at 600 °C [41]. The slightly higher D/G ratio indicated increased defects. Herein, D/G ratio remained similar, but one could note that the doublets were less resolved in the case of supported nanocatalysts. This suggests possible interactions between the biochar support and the immobilized nanocatalysts or possible metal-induced defects during pyrolysis. Indeed, the spectral region between D and G bands coincided with V bands assigned to sp<sup>2</sup> and sp<sup>3</sup> amorphous carbonaceous structures [43]. Convolution of the V, D, and G bands yielded less resolution and a decrease in the peak position difference (G–D) from 228  $\text{cm}^{-1}$  for B-CA to 213 (B-CA@CuNi) and 208 (B-CA@CuNi<sub>10/1</sub>)  $\text{cm}^{-1}$ .

### 3.1.2. Surface Morphology and Elemental Composition (SEM/EDX)

Figure 4 shows the SEM pictures of B-CA, B-CA@Ni, B-CA@CuNi, and B-CA@CuNi<sub>10/1</sub>. Besides a few pores at the surface of B-CA (~400 nm diameter), the CA-treated biomass yielded a biochar with wax-like surface (Figure 4a), similar to the OP biochar prepared at 400 °C for 15 min (see for example [21]). For B-CA@Ni (Figure 4b), about 100 nm size, spherical Ni NPs were visible. The NPs were dispersed all over the biochar surface but showed substantial agglomeration. Figure 4c–e displays SEM images of B-CA@CuNi at various magnifications. As can be seen, the biochar showed particles with undefined shapes (Figure 4c) with good dispersion of CuNi NPs (Figure 4d). Higher magnification showed localized 400 nm spherical agglomerates (Figure 4e). Similar good dispersion of bimetallic NPs was noted for B-CA@CuNi<sub>10/1</sub> (Figure 4f). Further zooming in showed raspberry-shaped CuNi<sub>10/1</sub> NPs of  $174 \pm 8$  nm size (Figure 4g).

EDX spectra are displayed in Figure 5. Only C, O, and Ni peaks were noted for B-CA@Ni (Figure 5a), but both Cu and Ni were visible at similar relative peak intensity for B-CA@CuNi (Figure 5b). In the case of 10-fold higher initial copper nitrate impregnation compared to nickel nitrate, the final B-CA@CuNi<sub>10/1</sub> exhibited very small Ni peak compared to Cu (Figure 5c).

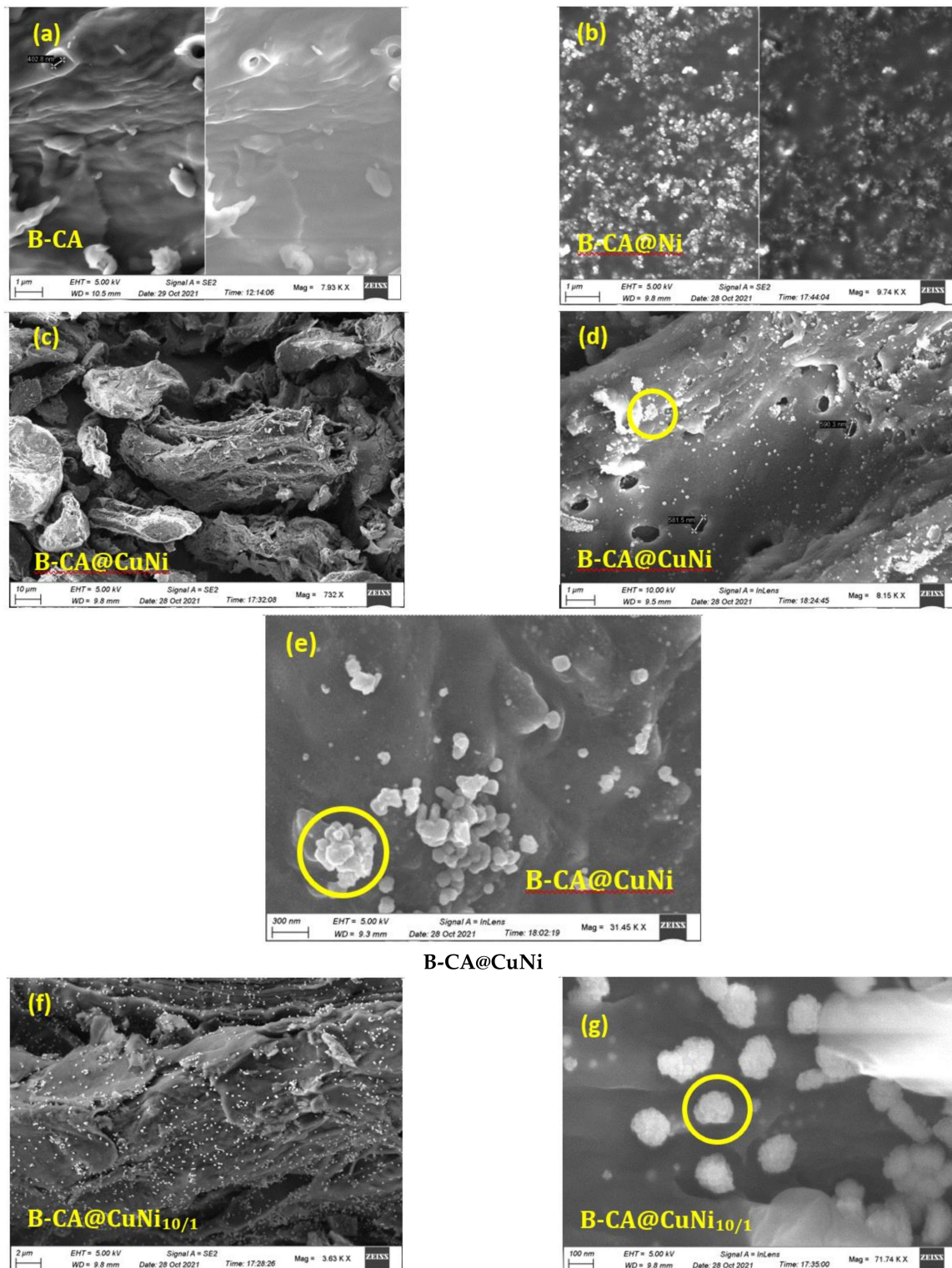


**Figure 4.** SEM images of (a) B-CA, (b) B-CA@Ni, (c–e) B-CA@CuNi, and (f,g) B-CA@CuNi<sub>10/1</sub>.

The Cu/Ni atomic ratio was found to be  $1.18 \pm 0.08$  and  $6.61 \pm 0.72$  for B-CA@CuNi and B-CA@CuNi<sub>10/1</sub> composites, respectively. For equal molar impregnation, while the Cu/Ni atomic ratio was close to 1 for B-CA@CuNi, the value was about 30% lower for the B-CA@CuNi<sub>10/1</sub> composite, possibly due to the existence of the most nickel-rich NPs, as judged from the XRD studies (Section 3.1.1).

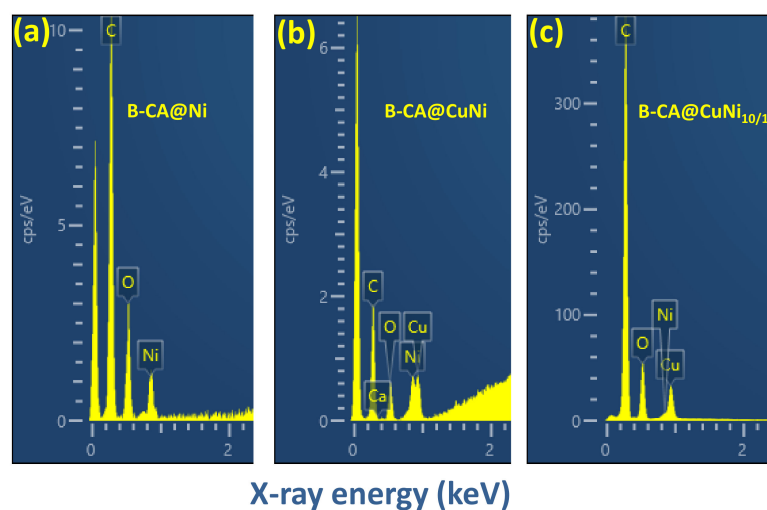


**Figure 5.** EDX spectra of (a) B-CA@Ni, (b) B-CA@CuNi, and (c) B-CA@CuNi<sub>10/1</sub>.

### 3.1.3. Magnetic Properties of Biochar Materials

The variation of the magnetization as a function of the magnetic field at RT is plotted for the three nickel-based biochar catalysts B-CA@CuNi, B-CA@CuNi<sub>10/1</sub>, and B-CA@Ni in Figure 6. A typical soft ferromagnetic behavior could be noted with a high-field magnetization, which decreased when the Ni content decreased, explaining why the most nickel-rich biochar was more easily attracted by an external magnetic field during the catalysis assays.

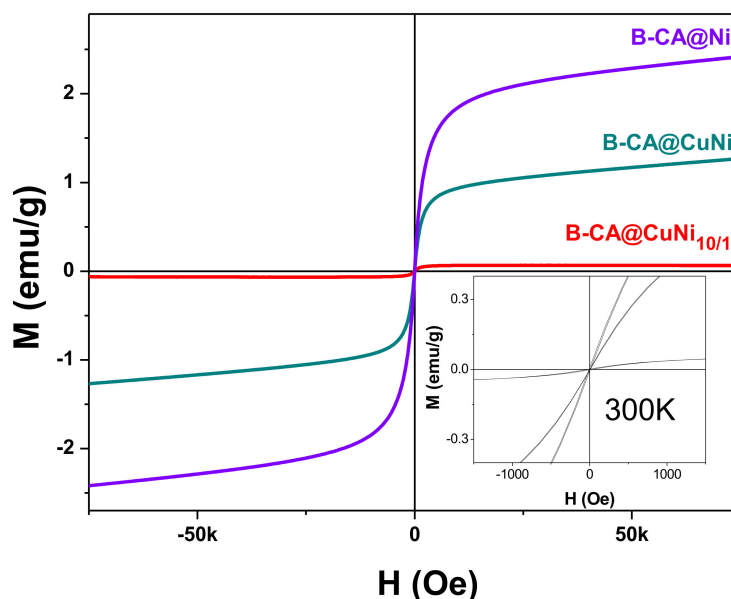


**Figure 6.** Magnetization of metallic nanoparticle-coated biochar versus the magnetic field at RT.

Interestingly, when expressed as per gram of nickel, the obtained high-field magnetization values were significantly lower than the expected 50 emu/g of bulk Ni, even for the copper-free, Ni-based catalyst (B-CA@Ni). This means that the major part of the involved nickel species corresponded to Ni<sup>2+</sup> instead of Ni<sup>0</sup>, without degradation of catalytic performance. This result is in agreement with that inferred from XRD and SEM/EDX analyses, which clearly showed that nickel was oxidized on the biochar surface, most probably upon exposure to air, following the pyrolysis process. It seems that the operating catalysis conditions, which required the introduction of NaBH<sub>4</sub> reducing agent into the reaction medium, allowed the Ni<sup>2+</sup> cations to be reduced into Ni<sup>0</sup> in situ, leading to the amount of available metal nickel surfaces being high enough to conduct the desired catalytic reaction.

Nonetheless, as noted in the video (see Supplementary Materials), B-CA@CuNi was attracted by the magnet to the sidewall of the beaker and returned to the center of the beaker upon withdrawal of the magnet. In contrast, B-CA@CuNi<sub>10/1</sub> was not attracted due to the low nickel loading on the biochar.

### 3.2. Potential Application: Degradation of Methyl Orange

The catalytic performance of B-AC@CuNi was tested, with the degradation of methyl orange (MO) chosen as a model reaction (Figure 7). As a first yes/no test, Figure 7a displays the MO UV–vis spectrum before and after catalytic discoloration resulting from the degradation of the dye. Discoloration was achieved in less than 10 min, which was much faster than the 30 min reported for the same type of composite but prepared in the absence of any citric acid [21]. This yes/no test was done with excess NaBH<sub>4</sub>.

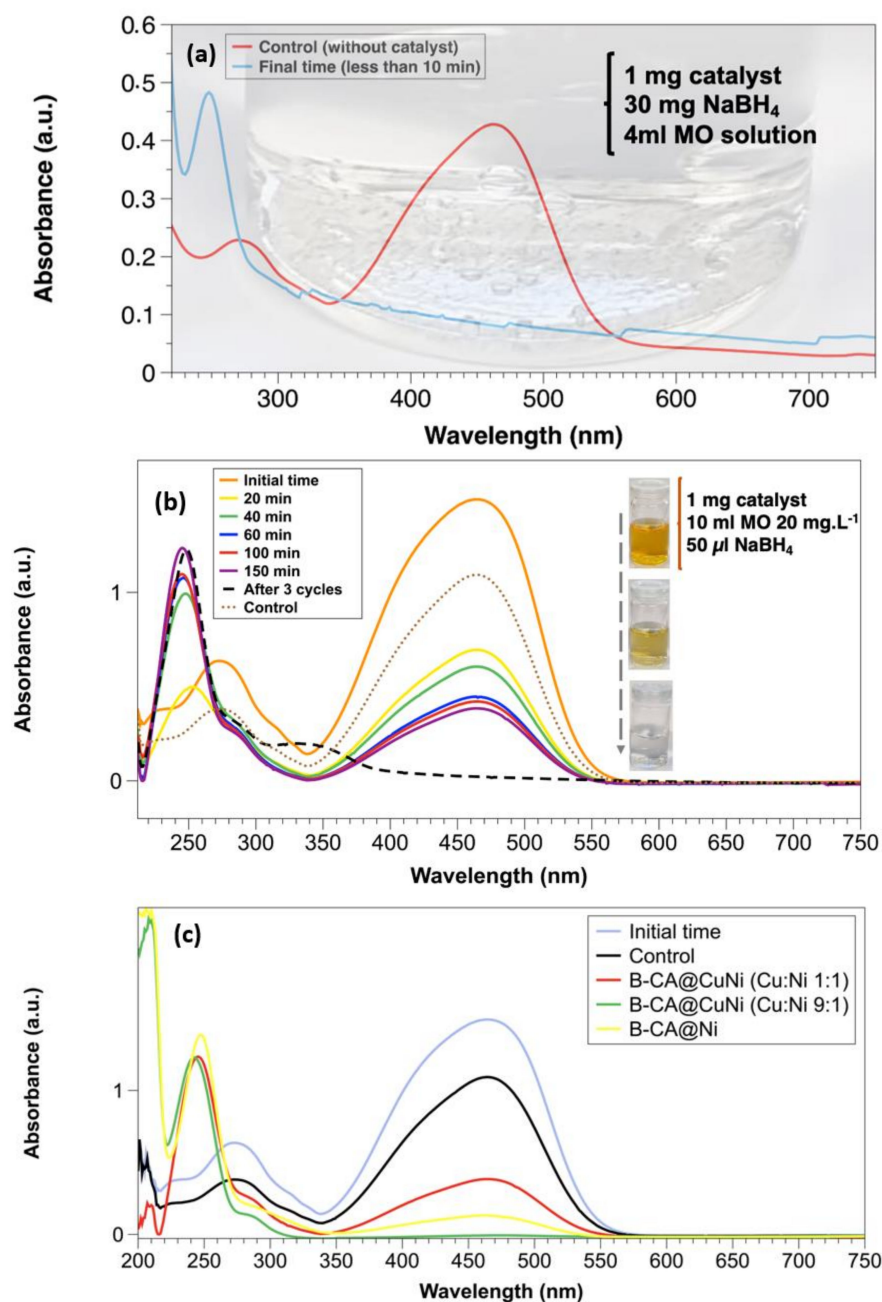


Figure 7. Cont.

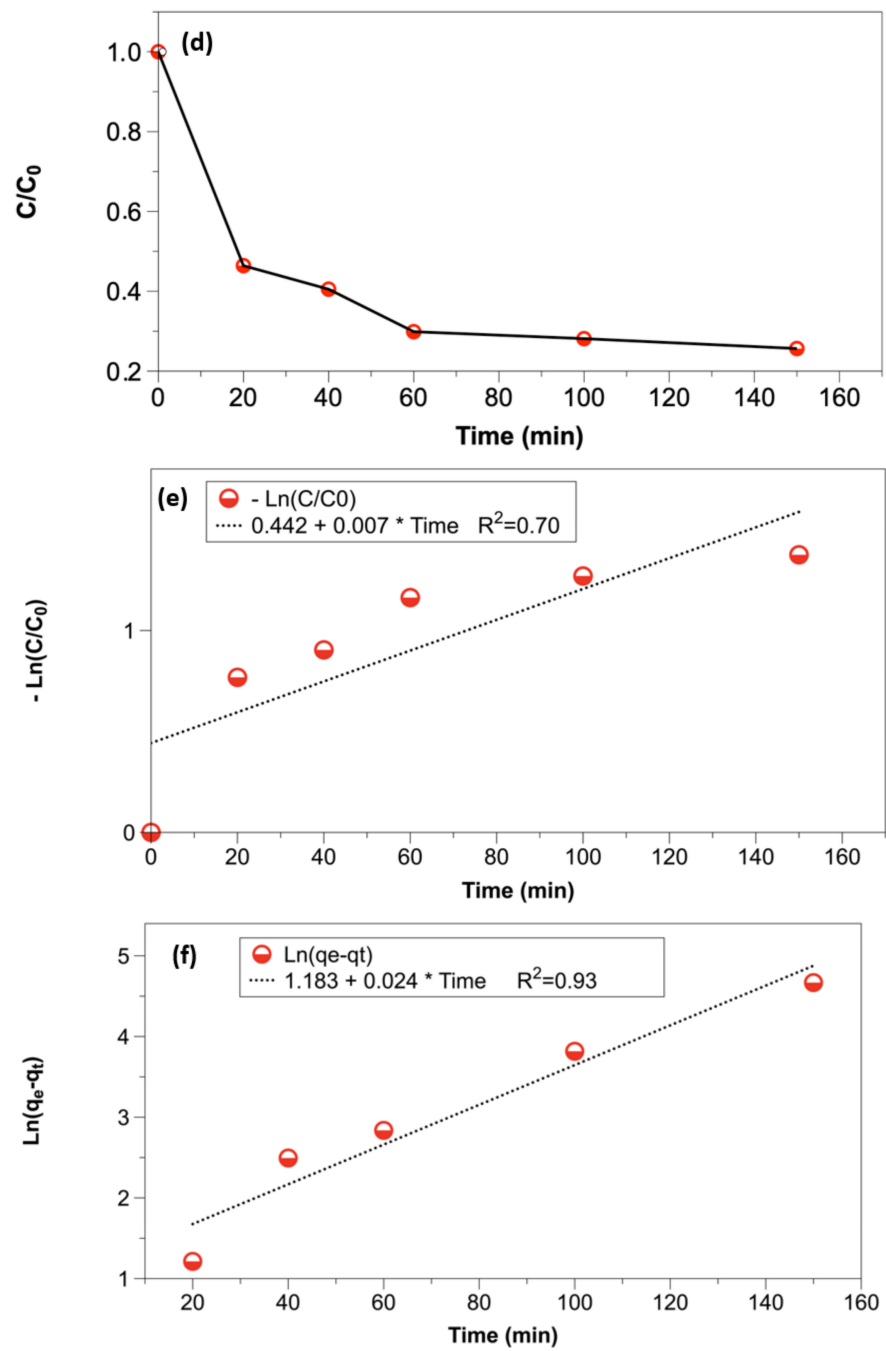
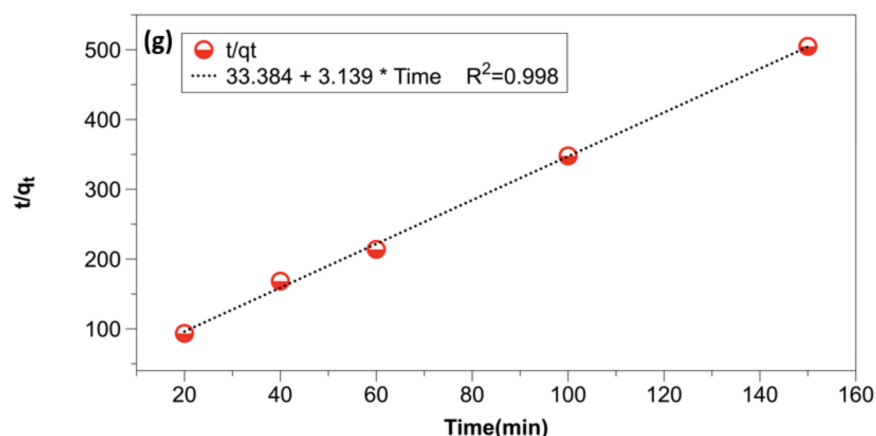


Figure 7. Cont.



**Figure 7.** Kinetic study of MO degradation: (a) fast test using excess  $\text{NaBH}_4$  ( $7.5 \text{ mg}\cdot\text{mL}^{-1}$ ), (b) stacked UV-vis spectra recorded using low  $\text{NaBH}_4$  concentration ( $0.38 \text{ mg}\cdot\text{mL}^{-1}$ ), (c) comparison of the performance of various biochar-based catalysts, (d)  $C/C_0$  vs. time plot for MO degradation, (e) first-order kinetics, (f) pseudo-first-order kinetics, and (g) pseudo-second-order kinetics. “Control” in (c) means test without any catalyst.

In order to establish the kinetic study and be able to monitor the variation of organic molecule concentration versus time, measurements were carried out with the following steps. First, 1 mg of the catalyst was dispersed in 10 mL of MO solution ( $20 \text{ mg}\cdot\text{L}^{-1}$  or 20 ppm) before adding 50  $\mu\text{L}$  of sodium borohydride solution (2M), which corresponded to the time  $t_0$ . The final mass of  $\text{NaBH}_4$  introduced to the reaction medium was 3.8 mg. However, herein, 3.8 mg was introduced in 10 mL instead of 30 mg in 4 mL for the fast yes/no test (about 8-fold less mass or 20-fold lower concentration of sodium borohydride).

As one can see in Figure 7b, as the orange color vanished, the intensity of the absorption peak at 463 nm decreased. In contrast, the intensity increase of the peaks centered at 247 and  $\sim 280$  nm. These two last peaks could be assigned to the two catalyzed degradation products of the dye.

It was practically difficult to collect 1 mg of the catalyst despite its high magnetic properties. To ensure reusability of 1 mg of B-AC@CuNi, 10 mL of the MO solution and 50  $\mu\text{L}$  of the  $\text{NaBH}_4$  2M solution were added each time after total disappearance of the initial orange color until three successive cycles were reached. This clearly indicated the robust immobilization of the bimetallic nanocatalyst on biochar without any significant leaching.

The final solution turned colorless and transparent, accompanied by total degradation of the azo dye (see dashed black line in Figure 7b). Figure 7c compares the performance of the biochar-based catalysts (NB: the control spectrum corresponds to the absence of any catalyst). The B-AC@Ni and B-CA@CuNi had comparable performance, whereas the B-CA@CuNi<sub>10/1</sub> induced faster reaction that was completed within 1 min. Note, however, that B-CA@CuNi<sub>10/1</sub> was not magnetic and could not be recovered by an external magnet. As far as the price is concerned, nickel nitrate is almost twice as more expensive than copper nitrate, regardless of the supplier.

The evolution of the ratio  $C/C_0$  versus  $t$ , shown in Figure 7d (and deduced from the processed peaks in Figure 7b), was characterized by three main phases: (i) fast degradation rate in the first 20 min, with almost 45% of MO being degraded; (ii) a slowdown in the degradation rate until 60 min, with degradation efficiency reaching 70%; and (iii) very slow turning during the last 90 min (the final degradation yield was 75%).

The fitting of the experimental data to the first, the pseudo-first, and the pseudo-second-order rate laws showed that the data did not fit the expected first-order or the pseudo-first-order model but excellently fit the pseudo-second-order model, which as-

sumed that the adsorption mechanism was chemisorption. It may be recalled that the linearized equations of the three models are given as follows:

$$\ln \frac{C}{C_0} = -K t \quad (1)$$

$$\ln(q_e - q_t) = \ln q_e - \frac{K_1}{2.303} t \quad (2)$$

$$\frac{1}{q_t} = \frac{1}{K_2 q_e^2} + \frac{1}{q_e} t \quad (3)$$

For the pseudo-first-order model (Equation (1)),  $K$  ( $\text{min}^{-1}$ ) is the apparent rate constant,  $C_0$  ( $\text{mg L}^{-1}$ ) is the initial concentration of MO, and  $C$  ( $\text{mg L}^{-1}$ ) is the concentration of the dye at time  $t$ . For the pseudo-first-order model (Equation (2)),  $K_1$  ( $\text{min}^{-1}$ ) is the equilibrium constant rate (the adsorption of MO over B-AC@CuNi), and  $q_t$  ( $\text{mg g}^{-1}$ ) and  $q_e$  ( $\text{mg g}^{-1}$ ) are the adsorbed amount at time  $t$  and at the equilibrium time, respectively. For the pseudo-second-order model (Equation (3)),  $K_2$  ( $\text{g mg}^{-1} \text{min}^{-1}$ ) is the equilibrium constant rate, and  $q_t$  and  $q_e$  are expressed in  $\text{mg L}^{-1}$  and  $\text{mg g}^{-1}$ , respectively.

The analyses of the experimental data according to the rate laws are displayed in Figure 7e–g.

A proposed degradation mechanism of MO in the presence of  $\text{NaBH}_4$  is illustrated in Figure 8. It is a two-step mechanism where the antibonding orbital of  $\text{H}_2$  generated after the reaction of sodium borohydride and water reacts with the unfilled d-bond of the metal to form dative bonding (between  $\text{H}_2$  and the metallic nanostructure) [44].

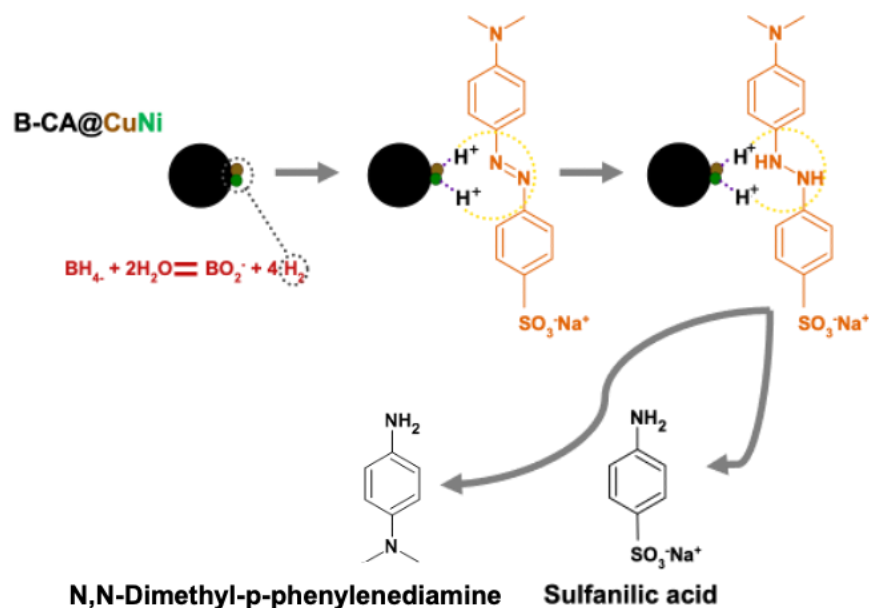


**Figure 8.** Proposed mechanism of degradation of MO using B-CA@CuNi in the presence of  $\text{NaBH}_4$ .

#### 4. Conclusions

Olive pit (OP) grains loaded with bimetallic CuNi nanoparticles were prepared by slow pyrolysis at  $400^\circ\text{C}$  under dinitrogen stream for 2 h. In this follow-up to our previous work [21], we investigated the effect of preimpregnation of OP grains with citric acid (CA) on the structural and morphological properties of the final B-CA@CuNi biochar. Contrary to the previous findings, herein, CA induced the formation of agglomerated metallic nanoparticles of nickel or its copper alloys. In particular, unusual raspberry-shaped nickel NPs were obtained in the case of B-CA@Ni. Moreover, more defects were noted for B-CA compared to the biochar prepared without CA as judged by the higher corresponding D/G ratio determined by Raman spectroscopy. From the crystallographic viewpoint, small

bimetallic NPs were formed, some with a nickel-rich phase. Small size readily induced metal oxidation of the supported NPs upon air exposure. B-CA@CuNi remained attracted by a magnet and was also able to catalyze the degradation of methyl orange in the presence of NaBH<sub>4</sub>. This compound could help reduce the formed metal oxides while participating in the catalyzed reaction. Discoloration of the dye was achieved with 1 mg of B-CA@CuNi and in the presence of a low amount of NaBH<sub>4</sub>. It was monitored by UV-vis spectrometry and, unexpectedly, was not found to fit a pseudo-first-order kinetics model.

This work conclusively shows that citric acid not only alters the properties of the biochar but also induces unusual structures of metallic or bimetallic copper/nickel or pure nickel nanocatalysts. These promising results encourage us to further investigate the effect of citric acid concentration on the shape and dispersion of (bi)metallic catalysts on biochar. This is valid for any other carboxylic acid.

**Supplementary Materials:** The following are available online <https://vimeo.com/563459182>, accessed on 16 February 2022.

**Author Contributions:** Conceptualization: M.M.C., A.M.K. and S.A.; methodology: M.M.C., A.M.K., Y.S. and S.A.; validation: all authors; formal analysis and investigation: all authors; writing—original draft: J.O. and M.M.C.; writing—review and editing: all authors; resources: M.M.C. and S.A.; supervision: M.M.C.; funding acquisition: A.M.K., A.K.B., S.A. and M.M.C. All authors have read and agreed to the published version of the manuscript.

**Funding:** A.M.K. and M.M.C. would like to thank both the French and Egyptian governments for funding A.M.K.'s contribution through a fellowship granted by the French Embassy in Egypt (Institut Francais d’Egypte) and Science and Technology Development Fund (STDF) Egypt, project number 42248. A.K.B. is also thankful to bourse WBI Excellence World (N° Imputation 101386 and Article Budgétaire 33.01.00.07).

**Institutional Review Board Statement:** Not applicable.

**Informed Consent Statement:** Not applicable.

**Data Availability Statement:** Original data available on request. They are not archived in any repository.

**Acknowledgments:** The authors would like to thank S. Gam-Derouich (experimental officer) for SEM/EDX analyses.

**Conflicts of Interest:** The authors declare no conflict of interest.

## References

1. Nanda, S.; Dalai, A.K.; Berruti, F.; Kozinski, J.A. Biochar as an exceptional bioresource for energy, agronomy, carbon sequestration, activated carbon and specialty materials. *Waste Biomass Valorization* **2016**, *7*, 201–235. [CrossRef]
2. Tripathi, M.; Sahu, J.N.; Ganesan, P. Effect of process parameters on production of biochar from biomass waste through pyrolysis: A review. *Renew. Sustain. Energy Rev.* **2016**, *55*, 467–481. [CrossRef]
3. Harussani, M.; Sapuan, S. Development of Kenaf Biochar in Engineering and Agricultural Applications. *Chem. Afr.* **2021**, *5*, 1–17. [CrossRef]
4. Atabani, A.; Ali, I.; Naqvi, S.R.; Badruddin, I.A.; Aslam, M.; Mahmoud, E.; Almomani, F.; Juchelková, D.; Atelge, M.; Khan, T.Y. A state-of-the-art review on spent coffee ground (SCG) pyrolysis for future biorefinery. *Chemosphere* **2022**, *286*, 131730. [CrossRef]
5. Sutar, S.; Patil, P.; Jadhav, J. Recent advances in biochar technology for textile dyes wastewater remediation: A review. *Environ. Res.* **2022**, *209*, 112841. [CrossRef]
6. Lu, Y.; Dai, T.; Fan, D.; Min, H.; Ding, S.; Yang, X. Turning Trash into Treasure: Pencil Waste-Derived Materials for Solar-Powered Water Evaporation. *Energy Technol.* **2020**, *8*, 2000567. [CrossRef]
7. Kumar, A.; Bhattacharya, T. Biochar: A sustainable solution. *Environ. Dev. Sustain.* **2021**, *23*, 6642–6680. [CrossRef]
8. Pan, X.; Gu, Z.; Chen, W.; Li, Q. Preparation of biochar and biochar composites and their application in a Fenton-like process for wastewater decontamination: A review. *Sci. Total Environ.* **2021**, *754*, 142104. [CrossRef]
9. Al-Wabel, M.I.; Al-Omran, A.; El-Naggar, A.H.; Nadeem, M.; Usman, A.R. Pyrolysis temperature induced changes in characteristics and chemical composition of biochar produced from conocarpus wastes. *Bioresour. Technol.* **2013**, *131*, 374–379. [CrossRef] [PubMed]

10. Eshun, J.; Wang, L.; Ansah, E.; Shahbazi, A.; Schimmel, K.; Kabadi, V.; Aravamudhan, S. Characterization of the physicochemical and structural evolution of biomass particles during combined pyrolysis and CO<sub>2</sub> gasification. *J. Energy Inst.* **2019**, *92*, 82–93. [[CrossRef](#)]
11. Leng, L.; Xiong, Q.; Yang, L.; Li, H.; Zhou, Y.; Zhang, W.; Jiang, S.; Li, H.; Huang, H. An overview on engineering the surface area and porosity of biochar. *Sci. Total Environ.* **2021**, *763*, 144204. [[CrossRef](#)]
12. Zhou, Y.; Qin, S.; Verma, S.; Sar, T.; Sarsaiya, S.; Ravindran, B.; Liu, T.; Sindhu, R.; Patel, A.K.; Binod, P. Production and beneficial impact of biochar for environmental application: A comprehensive review. *Bioresour. Technol.* **2021**, *337*, 125451. [[CrossRef](#)]
13. Xie, Y.; Wang, L.; Li, H.; Westholm, L.J.; Carvalho, L.; Thorin, E.; Yu, Z.; Yu, X.; Skreiberg, Ø. A critical review on production, modification and utilization of biochar. *J. Anal. Appl. Pyrolysis* **2022**, *161*, 105405. [[CrossRef](#)]
14. Plácido, J.; Bustamante-López, S.; Meissner, K.; Kelly, D.; Kelly, S. Microalgae biochar-derived carbon dots and their application in heavy metal sensing in aqueous systems. *Sci. Total Environ.* **2019**, *656*, 531–539. [[CrossRef](#)]
15. Barrientos, K.; Gaviria, M.I.; Arango, J.P.; Plácido, J.; Bustamante, S.; Londoño, M.E.; Jaramillo, M. Synthesis, Characterization and Ecotoxicity Evaluation of Biochar-Derived Carbon Dots from Spruce Tree, Purple Moor-Grass and African Oil Palm. *Processes* **2021**, *9*, 1095. [[CrossRef](#)]
16. Hidalgo, P.; Navia, R.; Hunter, R.; Coronado, G.; Gonzalez, M. Synthesis of carbon nanotubes using biochar as precursor material under microwave irradiation. *J. Environ. Manag.* **2019**, *244*, 83–91. [[CrossRef](#)]
17. Khalil, A.; Msaadi, R.; Sassi, W.; Ghanmi, I.; Michely, L.; Snoussi, Y.; Chevillot, A.; Lau-Truong, S.; Chehimi, M. Facile diazonium modification of pomegranate peel biochar: A stupendous derived relationship between thermal and Raman analyses. *ChemRxiv* **2021**. [[CrossRef](#)]
18. Wang, J.; Chen, N.; Li, M.; Feng, C. Efficient removal of fluoride using polypyrrole-modified biochar derived from slow pyrolysis of pomelo peel: Sorption capacity and mechanism. *J. Polym. Environ.* **2018**, *26*, 1559–1572. [[CrossRef](#)]
19. Endler, L.W.; Wolfart, F.; Mangrich, A.S.; Vidotti, M.; Marchesi, L.F. Facile method to prepare biochar–NiO nanocomposites as a promisor material for electrochemical energy storage devices. *Chem. Pap.* **2020**, *74*, 1471–1476. [[CrossRef](#)]
20. Qhubu, M.C.; Methula, B.; Xaba, T.; Moyo, M.; Pakade, V.E. Iron-Zinc Impregnated Biochar Composite as a Promising Adsorbent for Toxic Hexavalent Chromium Remediation: Kinetics, Isotherms and Thermodynamics. *Chem. Afr.* **2021**, 1–11. [[CrossRef](#)]
21. Khalil, A.M.; Michely, L.; Pires, R.; Bastide, S.; Jlassi, K.; Ammar, S.; Jaziri, M.; Chehimi, M. Copper/nickel-decorated olive pit biochar: One pot solid state synthesis for environmental remediation. *Appl. Sci.* **2021**, *11*, 8513. [[CrossRef](#)]
22. Lopes, R.P.; Astruc, D. Biochar as a support for nanocatalysts and other reagents: Recent advances and applications. *Coord. Chem. Rev.* **2021**, *426*, 213585. [[CrossRef](#)]
23. Tu, C.; Wei, J.; Guan, F.; Liu, Y.; Sun, Y.; Luo, Y. Biochar and bacteria inoculated biochar enhanced Cd and Cu immobilization and enzymatic activity in a polluted soil. *Environ. Int.* **2020**, *137*, 105576. [[CrossRef](#)] [[PubMed](#)]
24. Huang, W.-H.; Lee, D.-J.; Huang, C. Modification on biochars for applications: A research update. *Bioresour. Technol.* **2021**, *319*, 124100. [[CrossRef](#)]
25. Yang, Z.; Yang, R.; Dong, G.; Xiang, M.; Hui, J.; Ou, J.; Qin, H. Biochar nanocomposite derived from watermelon peels for electrocatalytic hydrogen production. *ACS Omega* **2021**, *6*, 2066–2073. [[CrossRef](#)]
26. Jing, H.; Ji, L.; Wang, Z.; Guo, J.; Lu, S.; Sun, J.; Cai, L.; Wang, Y. Synthesis of ZnO nanoparticles loaded on biochar derived from spartina alterniflora with superior photocatalytic degradation performance. *Nanomaterials* **2021**, *11*, 2479. [[CrossRef](#)]
27. Yang, X.; Zhang, S.; Ju, M.; Liu, L. Preparation and modification of biochar materials and their application in soil remediation. *Appl. Sci.* **2019**, *9*, 1365. [[CrossRef](#)]
28. Cheng, B.-H.; Zeng, R.J.; Jiang, H. Recent developments of post-modification of biochar for electrochemical energy storage. *Bioresour. Technol.* **2017**, *246*, 224–233. [[CrossRef](#)]
29. Shang, L.; Xu, H.; Huang, S.; Zhang, Y. Adsorption of ammonium in aqueous solutions by the modified biochar and its application as an effective N-fertilizer. *Water Air Soil Pollut.* **2018**, *229*, 320. [[CrossRef](#)]
30. Li, F.; Jin, Y.; He, S.; Jin, J.; Wang, Z.; Khan, S.; Tian, G.; Liang, X. Use of polyacrylamide modified biochar coupled with organic and chemical fertilizers for reducing phosphorus loss under different cropping systems. *Agric. Ecosyst. Environ.* **2021**, *310*, 107306. [[CrossRef](#)]
31. Mirzaei, P. Préparation de matériaux d'électrode pour l'élimination et la valorisation de polluants azotés. Ph.D. Thesis, Paris Est, Paris, France, 2018.
32. Liu, Y.; Deng, B.; Li, K.; Wang, H.; Sun, Y.; Dong, F. Metal-organic framework derived carbon-supported bimetallic copper-nickel alloy electrocatalysts for highly selective nitrate reduction to ammonia. *J. Colloid Interface Sci.* **2022**, *614*, 405–414. [[CrossRef](#)]
33. Yao, D.; Xu, T.; Yuan, J.; Tao, Y.; He, G.; Chen, H. Graphene based copper-nickel bimetal nanocomposite: Magnetically separable catalyst for reducing hexavalent chromium. *ChemistrySelect* **2020**, *5*, 3243–3247. [[CrossRef](#)]
34. Al-Enizi, A.M.; Ubaidullah, M.; Ahmed, J.; Alrobei, H.; Alshehri, S.M. Copper nickel@ reduced graphene oxide nanocomposite as bifunctional electro-catalyst for excellent oxygen evolution and oxygen reduction reactions. *Mater. Lett.* **2020**, *260*, 126969. [[CrossRef](#)]
35. Ismail, M.; Khan, M.; Khan, S.B.; Khan, M.A.; Akhtar, K.; Asiri, A.M. Green synthesis of plant supported CuAg and CuNi bimetallic nanoparticles in the reduction of nitrophenols and organic dyes for water treatment. *J. Mol. Liq.* **2018**, *260*, 78–91. [[CrossRef](#)]

36. Yuan, D.; Zhang, L.; Wan, S.; Sun, L. Rational design of microporous biochar based on ion exchange using carboxyl as an anchor for high-efficiency capture of gaseous p-xylene. *Sep. Purif. Technol.* **2021**, *286*, 120402. [[CrossRef](#)]
37. Sun, L.; Chen, D.; Wan, S.; Yu, Z. Performance, kinetics, and equilibrium of methylene blue adsorption on biochar derived from eucalyptus saw dust modified with citric, tartaric, and acetic acids. *Bioresour. Technol.* **2015**, *198*, 300–308. [[CrossRef](#)]
38. Shen, Y.; Zhang, N.; Zhang, S. Catalytic pyrolysis of biomass with potassium compounds for Co-production of high-quality biofuels and porous carbons. *Energy* **2020**, *190*, 116431. [[CrossRef](#)]
39. Zabiszak, M.; Nowak, M.; Taras-Goslinska, K.; Kaczmarek, M.T.; Hnatejko, Z.; Jastrzab, R. Carboxyl groups of citric acid in the process of complex formation with bivalent and trivalent metal ions in biological systems. *J. Inorg. Biochem.* **2018**, *182*, 37–47. [[CrossRef](#)]
40. Khemakhem, M.; Jaziri, M. Composites based on (ethylene–propylene) copolymer and olive solid waste: Rheological, thermal, mechanical, and morphological behaviors. *Polym. Eng. Sci.* **2016**, *56*, 27–35. [[CrossRef](#)]
41. Puig-Gamero, M.; Esteban-Arranz, A.; Sanchez-Silva, L.; Sánchez, P. Obtaining activated biochar from olive stone using a bench scale high-pressure thermobalance. *J. Environ. Chem. Eng.* **2021**, *9*, 105374. [[CrossRef](#)]
42. Li, X.; Hayashi, J.-I.; Li, C.-Z. Volatilisation and catalytic effects of alkali and alkaline earth metallic species during the pyrolysis and gasification of Victorian brown coal. Part VII. Raman spectroscopic study on the changes in char structure during the catalytic gasification in air. *Fuel* **2006**, *85*, 1509–1517. [[CrossRef](#)]
43. Pusceddu, E.; Montanaro, A.; Fioravanti, G.; Santilli, S.; Foscolo, P.; Criscuoli, I.; Raschi, A.; Miglietta, F. Comparison between ancient and fresh biochar samples, a study on the recalcitrance of carbonaceous structures during soil incubation. *Int. J. New Technol. Res.* **2017**, *3*, 39–46.
44. Chen, Z.-X.; Jin, X.-Y.; Chen, Z.; Megharaj, M.; Naidu, R. Removal of methyl orange from aqueous solution using bentonite-supported nanoscale zero-valent iron. *J. Colloid Interface Sci.* **2011**, *363*, 601–607. [[CrossRef](#)] [[PubMed](#)]